A&A 556, A114 (2013)
DOI: 10.1051/0004-6361/201321457

Astronomy & Astrophysics

The XMM deep survey in the CDF-S

VI. Obscured AGN selected as infrared power-law galaxies

N. Castelló-Mor[1], F. J. Carrera[1], A. Alonso-Herrero[1,⋆], S. Mateos[1], X. Barcons[1], P. Ranalli[2,3], P. G. Pérez-González[4,⋆⋆], A. Comastri[3], C. Vignali[5], and I. Georgantopoulos[2]

[1] Instituto de Física de Cantabria (CSIC-UC), 39005 Santander, Spain
e-mail: castello@ifca.unican.es
[2] Institute of Astronomy, Astrophysics, Space Applications and Remote Sensing, National Observatory of Athens, Palaia Penteli, 15236 Athens, Greece
[3] INAF – Osservatorio Astronomico di Bologna, via Ranzani 1, 40127 Bologna, Italy
[4] Departamento de Astrofísica, Facultad de CC. Físicas, Universidad Complutense de Madrid, 28040 Madrid, Spain
[5] Physics & Astronomy Department, University of Bologna, Viale Berti Pichat 6/2, 40127 Bologna, Italy

Received 12 March 2013 / Accepted 1 July 2013

ABSTRACT

Context. Accretion onto supermassive black holes is believed to occur mostly in obscured active galactic nuclei (AGN). Such objects are proving rather elusive in surveys of distant galaxies, including those at X-ray energies.
Aims. Our main goal is to determine whether the revised IRAC criteria of Donley et al. (2012, ApJ, 748, 142; objects with an infrared (IR) power-law spectral shape), are effective at selecting X-ray type-2 AGN (i.e., absorbed $N_{\rm H} > 10^{22}$ cm^{-2}).
Methods. We present the results from the X-ray spectral analysis of 147 AGN selected by cross-correlating the highest spectral quality ultra-deep *XMM-Newton* and the *Spitzer*/IRAC catalogues in the *Chandra* Deep Field South. Consequently it is biased towards sources with high S/N X-ray spectra. In order to measure the amount of intrinsic absorption in these sources, we adopt a simple X-ray spectral model that includes a power-law modified by intrinsic absorption at the redshift of each source and a possible soft X-ray component.
Results. We find 21/147 sources to be heavily absorbed but the uncertainties in their obscuring column densities do not allow us to confirm their Compton-Thick nature without resorting to additional criteria. Although IR power-law galaxies are less numerous in our sample than IR non-power-law galaxies (60 versus 87 respectively), we find that the fraction of absorbed ($N_{\rm H}^{\rm intr} > 10^{22}$ cm^{-2}) AGN is significantly higher (at about 3 sigma level) for IR-power-law sources (∼2/3) than for those sources that do not meet this IR selection criteria (∼1/2). This behaviour is particularly notable at low luminosities, but it appears to be present, although with a marginal significance, at all luminosities.
Conclusions. We therefore conclude that the IR power-law method is efficient in finding X-ray-absorbed sources. We would then expect that the long-sought dominant population of absorbed AGN is abundant among IR power-law spectral shape sources not detected in X-rays.

Key words. X-rays: galaxies – galaxies: active – infrared: galaxies – surveys

1. Introduction

Obscured active galactic nuclei (AGN) have attracted much attention for a few decades, partly because a significant fraction of the power from accretion onto black holes is believed to be shrouded by circumnuclear matter (e.g. Fabian 1999). Such a population of obscured AGN is expected to be a major contributor to the cosmic X-ray background (XRB; Gilli et al. 2007). Since X-rays come from very close to the central engine in AGN and X-ray emission is not severely contaminated by the host galaxy, X-ray surveys are often used as an efficient method for identifying reliable and fairly complete samples of AGN (Mushotzky 2004; Brandt & Hasinger 2005). Large numbers of AGN are found in deep X-ray surveys, where the observed AGN sky density is about an order of magnitude higher than that found at any other wavelength (e.g. Steidel et al. 2002; Bauer et al. 2004). These X-ray point sources can account for most of the observed XRB intensity at energies below 8 keV. X-ray surveys with *Chandra* and *XMM-Newton* have now resolved the totality of the XRB below ∼2 keV (e.g. Bauer et al. 2004; Mushotzky 2004; Hickox & Markevitch 2006). This fraction, however, drops to ∼50% at photon energies above 8 keV (Worsley et al. 2004, 2005). The majority of the X-ray point sources detected in the 2-8 keV band are moderately obscured AGN ($N_{\rm H} \lesssim 3 \times 10^{23}$ cm^{-2}; e.g. Szokoly et al. 2004; Barger et al. 2005; Tozzi et al. 2006; Mateos et al. 2005). On the other hand, an additional population of heavily obscured ($N_{\rm H} \gtrsim 3 \times 10^{23}$ cm^{-2}), or even Compton-Thick ($N_{\rm H} > 1.5 \times 10^{24}$ cm^{-2}) AGN at cosmological distances, which are missed by conventional quasar surveys, is required by AGN synthesis models of the XRB (e.g. Gilli et al. 2007; Treister et al. 2009; Luo et al. 2011). These are the best candidates to fill the residual 50% of the XRB above 8 keV, not accounted for by source populations in existing X-ray One fundamental ingredient in our understanding of the AGN population is the ratio of obscured to unobscured AGN, and how this ratio depends on parameters like intrinsic luminosity or redshift. Thus, a measurement

⋆ Augusto G. Linares Senior Research Fellow.
⋆⋆ Associate Astronomer at Steward Observatory, The University of Arizona, Tucson, AZ, USA.

of the fraction of obscured AGN and its possible dependence on critical parameter's can be used to study AGN structure and to probe the connection between AGN activity and formation of the host galaxy. The number density of these heavily obscured and Compton-Thick AGN is expected to outnumber unobscured AGN by a ratio of ∼2–4 : 1 (e.g. Maiolino & Rieke 1995; Comastri et al. 2001; Gilli et al. 2001, 2007; Xue et al. 2012), though the exact value is still not well constrained. Deep X-ray observations can only detect the most luminous of these hard X-ray sources, and even the deepest X-ray surveys likely miss large populations of heavily obscured AGN (Tozzi et al. 2006; Georgantopoulos et al. 2007, 2009; Comastri et al. 2011; Feruglio et al. 2011; Della Ceca et al. 2008). Thus, a significant fraction of the AGN population probably remains undetected even in X-rays.

According to the Unified AGN model, AGN are thought to have a dusty environment surrounding an optically and X-ray-bright accretion disc around a super-massive black hole ($M_{\rm BH} \gtrsim 10^6\,M_{\odot}$, e.g. Antonucci 1993; Urry & Padovani 1995). This dusty material is expected to be distributed in a torus-shaped structure centred in the super-massive black hole. The torus provides anisotropic obscuration of the central region so that sources viewed through a gas and dust-free line of sight are recognized as type-1 AGN, and those obscured by dust are classified as type-2 AGN, based on the characteristics of their optical spectra. Incident X-ray, optical and UV radiation from the central engine can be absorbed and reprocessed by the circumnuclear dust. An obscuring dusty torus should re-radiate in the infrared (IR) a significant fraction of the nuclear luminosity it absorbs, and the continua from most AGN indeed show significant IR emission (Barvainis 1987; Granato & Danese 1994; Nenkova et al. 2002). Galaxies dominated by AGN emission typically show a power-law ($f_\nu \propto \nu^\alpha$, where α is the spectral index) spectral energy distribution (SED) in those ranges, although with a variety of slopes (from $\alpha = -0.5$ up to $\alpha = -3$). While the power-law locus itself extends to bluer slopes, luminous AGN are expected to display red slopes of $\alpha \leq -0.5$ (Alonso-Herrero et al. 2006; Donley et al. 2007). Of course, this does not necessarily mean that the spectral index is the same in the near- and mid-IR. It has been recognized that the ultraviolet (UV) and optical continuum of luminous QSOs could be described with a power law that can continue all the way into the near-, mid-, and even far-IR (see, e.g., Neugebauer et al. 1979; Elvis et al. 1994). The power-law-like emission at short wavelengths ($0.1 \lesssim \lambda \lesssim 1\,\mu$m), which is an upturn towards the big blue bump tail comes from the AGN accretion disc. A broad continuum excess is detected in the near-IR continuum of galaxies in the rest frame at 2–5 μm (Lu et al. 2003; Helou et al. 2004; Magnelli et al. 2008), which is attributed to radiation reprocessed by the dusty torus. Clumpy torus models (Nenkova et al. 2008) predict nearly isotropic emission at IR wavelengths ≥12 μm for any torus model parameters.

Thus, the IR spectral range provides a powerful, complementary method for identifying AGN over a wide range of intrinsic obscuration that might not be detected in the X-ray band. Various IR selections have been employed extensively to search for AGN in which strong re-radiation from obscuring dust is expected (Rieke & Lebofsky 1981; Edelson & Malkan 1986; Lacy et al. 2004; Stern et al. 2005; Barvainis 1987; Pérez García et al. 1998; Alonso-Herrero et al. 2006; Mateos et al. 2012; Stern et al. 2012; Assef et al. 2013; Yan et al. 2013). With the *Spitzer* mission (Werner et al. 2004), deep mid-IR data in multiple bands have been obtained in various cosmological survey fields with the IR Array Camera (IRAC, Fazio et al. 2004) and Multiband Imaging Photometer (MIPS, Rieke et al. 2004) instruments. The *Spitzer*/IRAC power-law selection (Alonso-Herrero et al. 2006; Donley et al. 2007, 2012) chooses sources whose IRAC SEDs follow a power law over a wide range of slopes (α). This is because, galaxies dominated by AGN emission typically exhibit a characteristic red power-law SED across the IRAC bands due to the superposition of blackbody emission from the AGN-heated dust. A problem commonly encountered when studying AGN properties based on IR observations is the significant contribution of the host galaxy to the near- and mid-IR (Kotilainen et al. 1992; Alonso-Herrero et al. 1996; Franceschini et al. 2005). However, in high-luminosity objects where the AGN outshines the host galaxy by a large factor in the rest-frame optical and near- and mid-IR, this should not be the case.

In this paper, we attempt to find midly/heavily obscured AGN in the ultra-deep *XMM-Newton* observations (carried out at 2–10 keV) in the *Chandra* Deep Field South (CDF-S) based on an IR-colour selection. For the mid-IR, we use the deep data taken with *Spitzer*/IRAC at 3.6–8.0 μm in this field and catalogued by Pérez-González et al. (2008). We also compare the X-ray properties of the sources detected both in X-rays and in the four IRAC bands with and without a power-law-like continuum shape. The goal is to explore and quantify the efficiency in finding obscured ($N_{\rm H} > 10^{22}$ cm^{-2}) AGN within the X-ray-detected sources and especially whether it is effective at selecting type-2 AGN at some luminosity range when looking at X-ray emitting sources that display a power-law SED in the IR. Any discussion about the origin of the presumably more heavily obscured set of IR galaxies not detected in X-rays is beyond the scope of this paper. There are other papers in these series (Comastri et al. 2011; Iwasawa et al. 2012; Georgantopoulos et al. 2013) investigating the heavily obscured and Compton-Thick nature of the sources in this ultra-deep *XMM-Newton* data, using different spectral models and additional criteria, obtaining compatible results, as we will discuss below.

This paper is organized as follows. We describe the parent X-ray and IR catalogues in Sect. 2, and we explain our method to select sources with an IR power-law-shape (Donley et al. 2012). In Sect. 3, we present our X-ray spectral analysis of the sources and the spectral findings are discussed in Sect. 4. We discuss in more detail the absorption column density distribution and the obscured AGN fraction as a function of the intrinsic X-ray luminosity and the near- and mid-IR-continuum shape, in Sect. 5. We summarize our conclusions in Sect. 6. Throughout the paper errors are 90% confidence for a single parameter (i.e., $\Delta\chi^2 = 2.71$, Avni 1976), unless otherwise stated. We estimated the most probable value for the fractions using a Bayesian approach and the binomial distribution from Wall & Jenkins (2008) for which the quoted errors are the narrowest interval that includes the mode and encompasses 90% of the probability. We assume the concordance cosmological model with $H_0 = 70.5$ km s^{-1} Mpc^{-1}, $\Omega_{\rm M} = 0.27$, and $\Omega_\Lambda = 0.73$ (Komatsu et al. 2009).

2. Sample

To study the X-ray properties of a sample of IR power-law AGN in the CDF-S and the Extended CDF-S (E-CDF-S) fields using ultra-deep *XMM-Newton* observations we took advantage of the deep *Spitzer* images available in that region. The CDF-S and the E-CDF-S areas were surveyed with *XMM-Newton* during different epochs spread over almost nine years (see Ranalli et al. 2013 for more details). The average Galactic column density towards the CDF-S is 0.9×10^{20} cm^{-2} (Dickey & Lockman 1990)

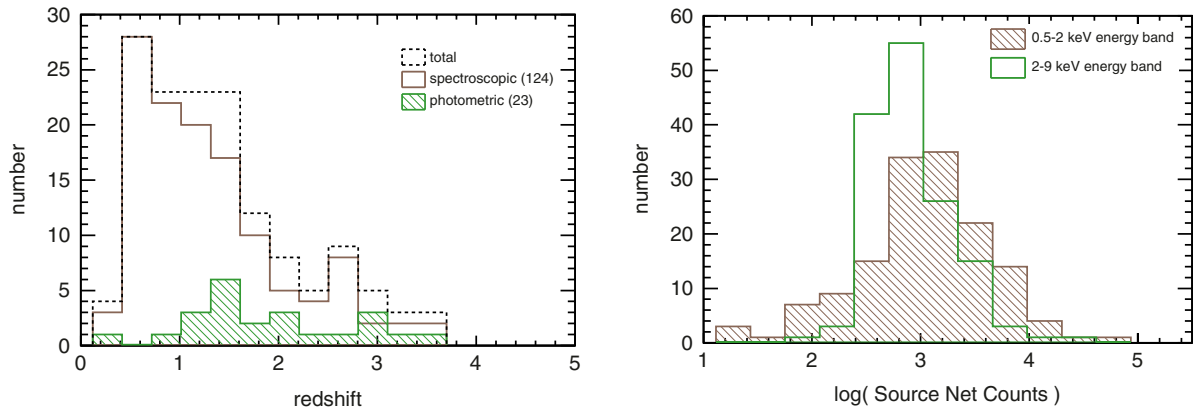

Fig. 1. *Left*: spectroscopic and photometric redshift distribution as solid-line and hatched histograms, respectively. The dashed-line histogram represents the distribution of the redshift, regardless of whether it is photometric or spectroscopic. *Right*: source net count distribution for both the 0.5–2 keV and 2–9 keV energy bands as hatched and empty histograms, respectively.

providing a relatively clean vision of the extragalactic X-ray sky even down to soft X-ray energies.

2.1. Infrared

The near- and mid-IR source catalogue used for this work has been built from *Spitzer*/IRAC observations (the selection being made at 3.6 μm and 4.5 μm). The total surveyed area is 664 arcmin^2. This IRAC sample is 75% complete down to 1.6 μJy. The data are described in detail in Pérez-González et al. (2008). A total of 23 044 non-flagged IRAC sources are selected from this sample with a high signal-to-noise ratio ($S/N > 5$) in each of the four bands (3.6, 4.5, 5.8, and 8.0 μm).

2.2. X-rays

The X-ray data presented in this paper were obtained from the CDF-S *XMM-Newton* survey. An extended and detailed description of the full data set, including the data analysis and reduction as well as the X-ray catalogue will be published in Ranalli et al. (2013). Briefly, the bulk of the X-ray observations were made between July 2008 and March 2010, and were combined with archival data taken between July 2001 and January 2002. The total net integration time (after removal of background flares) is ∼2.8 Ms and ∼2.5 Ms for the EPIC MOS and pn detectors, respectively. Standard *XMM-Newton* software and procedures were used for the analysis of the data. The source catalogue we use for this paper contains X-ray sources detected in the 2–10 keV band with conservative detection criteria: >8σ PWXDetect significance and an exposure time >1 Ms. These requirements resulted originally in 171 X-ray-detected sources. We then sub-selected the 150 objects for which spectral data are available for at least one of the three EPIC cameras: pn, MOS1 or MOS2 (see Comastri & the XMM-CDFS team 2013 for more information about the definition of the spectral catalogue). The exclusion of these 21 sources, spanning a wide range of redshift up to $z \sim 3$, does not intruduce any additional bias. Finally, we excluded 3 further objects for which the redshift is unknown. Our final X-ray sample contained then 147 AGN with spectroscopic and/or photometric redshifts, all with >180 counts in the observed 0.5–9 keV energy band. We note that the sample is not statistically complete as a result of the primary selection criteria, however, the aim of the paper is independent of any selection bias.

Hereafter we use "ID210 = for the identification number of X-ray sources listed in Ranalli et al. (2013). Spectroscopic redshifts are available for 124 objects while photometric redshifts were estimated by various papers for 23 further objects. The photometric and spectroscopic redshifts adopted in this paper are taken from Ranalli et al. (2013). The redshift distribution of the sample is shown in Fig. 1. The median redshift is 1.40. The distribution of the net (i.e., background subtracted) source counts in both the 2–9 keV and 0.5–2 keV energy bands are also given the same figure.

A classification purely based on optical properties has not been possible for the majority of the sources. Correlations between optical and X-ray properties of obscured and unobscured AGN show a very good match (∼80% or more) between optical reddening and X-ray absorption (e.g., Tozzi et al. 2006; Page et al. 2003; Perola et al. 2004). Usually, relatively low S/N unabsorbed AGN X-ray spectra are fit by simple power law models. The effect of increasing column density is that the soft part of the spectrum is more and more suppressed due to photometric absorption, i.e., the spectrum becomes harder at high $N_{\rm H}$. It is customary to define an X-ray unabsorbed AGN by $N_{\rm H} < 10^{22}$ cm^{-2}, whereas absorbed AGN satisfy $N_{\rm H} \geq 10^{22}$ cm^{-2}. This "borderline" value is a rather conservative upper limit to the amount of absorbing gas across the interstellar medium of a typical host galaxy's line of sight.

2.3. Cross-correlation

To identify X-ray/IR associations, we analysed the CDF-S ultra-deep *XMM-Newton* observations covering the sky positions of the IRAC catalogue. We crosscorrelated both catalogues applying the method developed by Pineau et al. (2011). The method is based on a likelihood ratio (LR) technique. For a given source, this method provides the probability of association for each candidate counterpart, which is a function of the positional errors, relative distance and the local density of potential counterparts. The much higher density of IRAC sources with respect to that of *XMM-Newton* sources and the large uncertainties in the *XMM-Newton*'s positions make this cross-correlation exercise particularly difficult. To facilitate our task, we used the cross-correlation between CDF-S *XMM-Newton* and the extended CDF-S *Chandra* catalogue (Ranalli et al. 2013) as a first step to find the CDF-S *XMM-Newton* counterparts to our IRAC targets. The reason for this is that the positions of the *Chandra* sources are much more accurate (a fraction of an arcsec) than those from

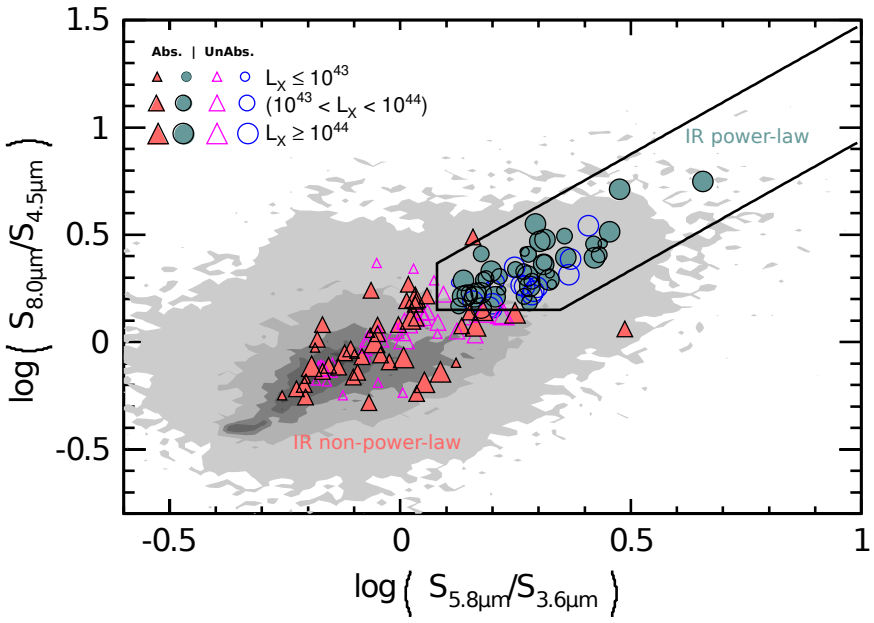

Fig. 2. IRAC colour–colour diagram for the entire IRAC sample (plotted as a surface grey map) and for the cross-correlation sample: blue circles and red triangles represent IR power-law and IR non-power-law galaxies according to Donley et al. (2012), respectively. The filled and empty symbols denote absorbed and unabsorbed sources, respectively. The symbols change in size to denote different ranges of X-ray luminosity. The solid line shows the revised IRAC-criteria wedge by Donley et al. (2012).

XMM-Newton (several arcsec, Lehmer et al. 2005; Xue et al. 2011), while the densities of both *Chandra* and *XMM-Newton* catalogues are similar. In practice this means that the associations between *Chandra* and *XMM-Newton* X-ray sources are highly reliable and this step does not introduce any uncertainty in our process to associate *XMM-Newton* to IRAC sources. We then use the *Chandra*'s positions instead of the less accurate *XMM-Newton* positions to search for IRAC counterparts.

Spitzer/IRAC data cover very well over 95% of the *XMM-Newton* exposure area used in this work. Only 6 X-ray sources fall in regions where there is partial or no coverage by the *Spitzer*/IRAC catalogue data. The catalogue of IR sources used is a compilation resulting from a number of different *Spitzer*/IRAC surveys in the E-CDF-S area, of different depths. We found one single IRAC counterpart for each X-ray source, and therefore our final sample contains 147 cross-correlations with a single counterpart. Thus, all sources have an X-ray spectrum from the CDF-S *XMM-Newton* observations, *Spitzer*/IRAC fluxes in the 4 bands and a spectroscopic or photometric redshift. The mean value X-ray-*Chandra*-IRAC source separation is $\lesssim$1.5 arcsec. We also estimate a fraction of spurious matches of randomized IRAC and X-ray sources of <1.5% (i.e., <2 sources in our case) from the cross-matching of IRAC and X-ray sources using a large offset in IRAC coordinates (3 arcmin in either RA or Dec).

2.4. Selection of IR power-law galaxies

Among all available IR-based colour selections of AGN, to construct the IR power-law sample we used the IR colour-based selection of AGN presented in Donley et al. (2012), which has been optimized to be both effective and extremely reliable in identifying luminous AGN. Donley et al. (2012) redefined the AGN selection criteria for deep IRAC surveys using large samples of luminous AGN and high-redshift star-forming galaxies in COSMOS. Although this revised IRAC criterion is extremely sensitive to the reliability of the photometric estimates, it has been designed to minimize the contaminants, such as high-redshift star-forming galaxies, which are otherwise present in other high-redshift galaxy samples of IR-based AGN candidates (e.g., Lacy et al. 2004; Stern et al. 2005).

The revised AGN selection by Donley et al. (2012) is defined by the following wedge,

$$x = \log\left(\frac{f_{\nu,5.8\ \mu m}}{f_{\nu,3.6\ \mu m}}\right), \quad y = \log\left(\frac{f_{\nu,8.0\ \mu m}}{f_{\nu,4.5\ \mu m}}\right)$$

$$x \geq 0.08 \quad \text{and} \quad y \geq 0.15 \quad \text{and}$$

$$y \geq (1.21 \times x) - 0.27 \quad \text{and} \quad y \leq (1.21 \times x) + 0.27 \quad \text{and}$$

$$f_{\nu,3.6\ \mu m} < f_{\nu,4.5\ \mu m} < f_{\nu,5.8\ \mu m} < f_{\nu,8.0\ \mu m}.$$

Following these criteria, we can directly obtain an IR-based classification: IR power-law are those lying within the revised IRAC-selection wedge and their IRAC SEDs are monotonically-rising within the IR bands. Thus, we label as IR non-power-law those galaxies, which fall outside the Donley et al. (2012)'s wedge and all the sources with non-monotonically-rising IRAC SEDs. The latter largely removes any possible contamination due to low-redshift star-forming galaxies (which would have little X-ray emission) in which their 1.6 μm stellar bump passes through the IRAC bandpass. Using these criteria, the IR power-law sample contains 60 X-ray-detected objects while the IR non-power-law sample consists of 87 X-ray-detected sources.

Hereafter, we concentrate on the X-ray spectral properties of these 147 X-ray-detected galaxies, highlighting possible differences between these two sub-samples (IR power-law and IR non-power-law). The main aim of this work is to investigate their intrinsic absorption distribution approaching the Compton-Thick limit and specially, to infer whether obscured AGN are the major contributor to the IR power-law-selected AGN survey or not, and specifically whether it is effective at selecting type-2 AGN at some luminosity range. By design, we cannot address in this paper the question of the nature of the IR power-law X-ray-undetected sources. Figure 2 shows the IRAC colour distribution for the entire IRAC sample. The colour symbols are our 147 X-ray-detected sources, with the blue circles showing the IR power-law galaxies and the red triangles the IR non-power-law objects. Filled and empty symbols denote absorbed ($N_{\rm H}^{\rm intr} > 10^{22}$ cm^{-2}) and unabsorbed ($N_{\rm H}^{\rm intr} \leq 10^{22}$ cm^{-2}) sources, respectively (see Sect. 5). The symbols also change in size to denote different ranges of the rest-frame 2–10 keV intrinsic luminosity.

3. X-ray spectral analysis

We have carried out an X-ray spectral analysis for the 147 sources with background-subtracted EPIC counts in the 0.5–9 keV band above 180. The *XMM-Newton* data were grouped to have at least 20 counts in each bin in order to apply the modified χ^2 minimization technique.

The ability to obtain a reliable fit depends on the X-ray spectral quality, or, in simpler terms, on the S/N of the X-ray spectrum under analysis. The distribution of the net counts in the 2–9 keV band for all the sources in our sample peaks at ∼700 (see Fig. 1). Despite the relatively high mean value of the net counts in the hard energy band, there are many cases in which the spectrum is dominated by the background. Therefore, the strategy for the X-ray spectral analysis must be appropriate for the high background regime.

A complete and detailed X-ray spectral analysis of the full sample of X-ray sources in the CDFS *XMM-Newton* survey is beyond the scope of this paper and will be presented in Comastri & the XMM-CDFS team (2013).

3.1. Spectral models

We carried out the spectral fitting of the 147 sources using *XSPEC* v 12.7.0 (Arnaud 1996). We started with a joint fitting of MOS and pn spectra with a power-law model (model `A`, see Table 3) with fixed Galactic absorption. The Galaxy H column density values for each X-ray source were obtained using the ftool *nh*[1], which interpolates over values from the HI map of Dickey & Lockman (1990). The MOS and pn spectral parameters were tied to the same value, while the normalisations were left free to vary in order to account for flux cross-calibration discrepancies between the EPIC MOS and pn cameras (Mateos et al. 2009). An additional component was included in addition to the power-law model to search for intrinsic rest-frame absorption: a redshifted neutral absorption by cold matter with redshift fixed to the source's spectroscopic or photometric value (model `C`, see Table 3). In a few cases (5/147), the resulting photon index is $\lesssim$1 (even when accounting for uncertainties), which is much lower than the typical values for unabsorbed AGN. A possible explanation would be that sources with such an observed flat spectrum were Compton-Thick AGN in which all the direct emission is suppressed and only reflected emission is observed at energies below 10 keV. However, this explanation does not seem to be valid because in all such cases. We find a significant amount of absorption but not in the Compton-Thick regime ($N_{\rm H}^{\rm intr}$'s between 10^{22} and a few 10^{23} cm^{-2}). The iron Kα emission line is not detected within sensitive limits (>3σ level). Our adopted explanation for the sources with an apparent very flat X-ray spectral index is the combination of a moderate absorption with poor statistics and/or high background (see, however, Georgantopoulos et al. 2013 where a more thorough examination of these sources yielded some Compton-Thick candidates). In those cases, an upper limit for the absorption is given at 90% level by freezing the spectral index at 1.9, which is the average value for unabsorbed AGN (Caccianiga et al. 2004; Mateos et al. 2005, 2010; Galbiati et al. 2005; Tozzi et al. 2006).

In other cases, the fit with a simple absorbed/unabsorbed power law is not a good description of the X-ray spectrum. Despite the fact that the high background regime does not allow us to investigate more complex spectral models as often present in AGN, we identify one possible additional spectral component: a soft X-ray excess. In this paper we have adopted a simple parametrisation for this component and we have only modelled it in the two simplest ways: one as a thermal emission (model `B` or `D`, see Table 3) from a collisionally ionized plasma, which is heated by shocks induced by AGN outflows (e.g. King 2005) or intense star formation (e.g. Schurch et al. 2002); and the other one as a power-law-like emission (model `E`, see Table 3) to account for the spectral complexity observed in some of our sources and which may not be well fit by a simple thermal emission.

Strongly obscured AGN can show a reflection-dominated spectrum and/or a high equivalent width iron line. These spectral features can be used as additional criteria to signpost Compton-Thick AGN (as in e.g. Georgantopoulos et al. 2013; Comastri & the XMM-CDFS team 2013). These kinds of Compton-Thick AGN would not necessarily be identified unambiguously as such in our analysis.

We performed the fits in the energy range 0.5–9 keV. We ignore the data below 0.5 keV to avoid uncertainties in the EPIC calibration. The 1.4–1.6 keV energy range was ignored to avoid any contribution from the Al-K fluorescence line in the internal *XMM-Newton* EPIC background. At high energies, the efficiency of *XMM-Newton* decreases rapidly and the energy bins >9 keV are dominated by noise and background for most sources.

We measured the significance of the detection of additional components in the X-ray spectra of our sources using the F-test statistic. The F-test measures the significance of a decrease in χ^2 when new components are added to the model. We used significance thresholds of 95% to accept the detection of soft excess and/or intrinsic absorption. In three sources, the temperature of the soft X-ray excess component of the best-fit model is far too high (>10 keV) to render this spectral component physically plausible. We consequently adopted as the best fit the one that yielded the least uncertain model parameters (provided that the values of these parameters are physically plausible).

4. Spectral results

Table 1 shows the best-fit model parameters for each object and the overall properties of the whole galaxy sample and the two subsamples are presented in Table 2. A summary of the models required during the spectral fit is summed up in Table 3. We also show a examples of fitted spectra for each component in Fig. 3. Finally, Fig. 4 displays the distribution of some model parameters of our sample, as computed from the best-fit model: the rest-frame X-ray power-law photon index, the intrinsic absorption column density, the observed 2–10 keV fluxes, and the 2–10 keV rest-frame luminosity corrected for both intrinsic and Galactic absorption. Whilst the solid-line hatched and empty histograms show the distribution for IR power-law and IR non-power-law galaxies, respectively, the dashed-line empty histogram shows the distribution for the whole sample. As we can see in the Figure, It is clear that IR power-law galaxies are distinct among the whole sample in several respects, as we shall see in the following subsections.

– *Soft X-ray component.*
Among the whole sample, only 33 sources ($\sim 22^{+6}_{-2}$%) have a soft emission component (`B`, `D`, and `E` models). In the full X-ray spectral analysis presented in Comastri & the XMM-CDFS team (2013) the origin of this soft X-ray emission component is studied in more detail. We note that the low fraction of sources with a significant soft X-ray component may be due to the high redshift of our sources

[1] http://heasarc.nasa.gov/lheasoft/ftools

Table 1. Details of the X-ray sources with IRAC counterpart found in this analysis presented in three panels.

PID (1)	z (2)	F_X (3)	L_X (4)	Γ (5)	N_H^{intr} (6)	KT (7)	model (8)	IRpl (9)	$N_H^{intr} CL(1\sigma)$ (10)	class (11)
2	1.622	9.89	195.68	$2.1\pm^{0.1}_{0.1}$	–	–	A	✓	0.02–0.17	*u*
3	1.59	4.20	64.01	$1.9\pm^{0.4}_{0.4}$	$8.37\pm^{3.83}_{2.84}$	–	C	✗	7–11	*a*
6	0.526	9.15	8.48	$1.6\pm^{0.1}_{0.1}$	–	$0.067\pm^{0.024}_{0.021}$	B	✓	≤0.04	*u*
13	1.05	4.19	16.42	$1.4\pm^{0.4}_{0.3}$	$0.86\pm^{0.96}_{0.75}$	–	C	✗	0.63–1.10	–
19	0.662	6.00	10.16	$1.7\pm^{0.3}_{0.3}$	$1.57\pm^{0.58}_{0.56}$	–	C	✗	1–3	*a*
21	1.156	3.68	22.15	$1.7\pm^{0.2}_{0.2}$	$3.04\pm^{2.86}_{1.81}$	–	C	✗	1–6	*a*
24	1.368	2.67	34.46	$1.9\pm^{0.2}_{0.2}$	$29\pm^{27}_{15}$	–	C	✗	20–50	*a*
26	3.198	2.73	239.94	$1.9\pm^{0.2}_{0.2}$	$46\pm^{59}_{29}$	–	C	✓	28–70	*a*
30	1.94	9.86	204.64	$1.5\pm^{0.1}_{0.1}$	$77\pm^{60}_{36}$	–	C	✗	400–1400	*a*
31	2.583	7.67	176.62	$1.3\pm^{0.1}_{0.1}$	–	–	A	✓	3–7	*a*
33	1.843	35.02	637.08	$1.7\pm^{0.0}_{0.1}$	–	$0.224\pm^{0.072}_{0.068}$	B	✓	2–4	*a*
34	1.63	1.13	9.08	1.9†	$82\pm^{36}_{30}$	–	C	✓	500–1200	*a*
37	0.624	3.75	10.21	1.9†	$20\pm^{11}_{8}$	–	C	✗	10–30	*a*
38	1.598	9.37	129.04	$1.8\pm^{0.1}_{0.1}$	–	–	A	✓	≥0.24	–
40	0.512	4.58	4.43	$1.9\pm^{0.2}_{0.2}$	–	–	A	✗	0.02–0.11	*u*
42	0.619	3.01	4.71	$1.9\pm^{0.2}_{0.2}$	$0.21\pm^{0.17}_{0.16}$	–	C	✗	0.05–0.38	*u*
43	1.167	3.89	24.80	$1.8\pm^{0.1}_{0.1}$	–	–	A	✗	≤0.05	*u*
44	1.51	3.45	22.13	$1.1\pm^{0.3}_{0.3}$	–	–	A	✗	≥0.03	–
45	0.717	4.23	7.67	$1.6\pm^{0.1}_{0.1}$	–	–	A	✗	0.10–0.24	*u*
48	0.298	42.64	11.94	$1.5\pm^{0.1}_{0.1}$	$4.36\pm^{0.81}_{0.62}$	$0.242\pm^{0.081}_{0.049}$	D	✗	4.6–5.7	*a*
49	2.298	4.55	103.95	$1.5\pm^{0.3}_{0.3}$	$3.43\pm^{1.86}_{1.23}$	–	C	✓	1.6–5.7	*a*
50	1.218	3.65	26.88	$1.8\pm^{0.3}_{0.3}$	$2.16\pm^{1.23}_{0.95}$	–	C	✗	1.2–3.4	*a*
57	2.571	2.71	184.29	$2.2\pm^{0.1}_{0.1}$	–	–	A	✓	≤0.08	*u*
60	1.049	3.78	17.66	$1.6\pm^{0.2}_{0.2}$	$4.24\pm^{1.73}_{1.42}$	–	C	✗	2.8–6.0	*a*
62	2.561	6.51	369.28	$2.0\pm^{0.1}_{0.1}$	–	$0.278\pm^{0.119}_{0.130}$	B	✓	14–48	*a*
64	3.34	6.75	327.35	$1.4\pm^{0.2}_{0.2}$	$70\pm^{44}_{31}$	–	C	✓	39–110	*a*
66	1.185	6.25	112.48	$1.9\pm^{0.2}_{0.2}$	$143\pm^{139}_{101}$	–	C	✗	43–280	*a*
68	2.005	6.99	173.27	$1.9\pm^{0.1}_{0.1}$	–	–	A	✗	≥0.3	–
71	0.494	3.99	4.53	$2.3\pm^{0.6}_{0.5}$	$2.30\pm^{3.47}_{0.92}$	$0.135\pm^{0.712}_{0.098}$	D	✓	2.2–4.1	*a*
72	0.839	3.31	11.09	$2.0\pm^{0.3}_{0.3}$	$1.47\pm^{0.43}_{0.52}$	–	C	✗	1.0–2.0	*a*
78	0.737	17.06	44.77	$1.7\pm^{0.3}_{0.3}$	$16\pm^{4}_{3}$	–	C	✗	12–20	*a*
81	1.887	17.70	311.20	$1.6\pm^{0.1}_{0.1}$	–	$0.411\pm^{0.059}_{0.077}$	B	✓	≥0.24	–
84	2.561	2.44	88.87	$1.7\pm^{0.4}_{0.4}$	$14\pm^{8}_{8}$	–	C	✗	8.0–23	*a*
89	1.271	5×10^{-4}	0.009	$1.3\pm^{0.4}_{0.4}$	$12\pm^{8}_{5}$	–	C	✓	16–26	*a*
92	3.42	1.15	176.05	$2.2\pm^{0.4}_{0.4}$	$19\pm^{11}_{8}$	–	C	✗	11–30	*a*
93	2.81	2.48	122.41	$1.7\pm^{0.6}_{0.5}$	$19\pm^{14}_{10}$	–	C	✓	8.4–33	*a*
95	1.17	5.29	71.49	$2.1\pm^{0.2}_{0.2}$	$65\pm^{30}_{20}$	–	C	✗	46–77	*a*
96	0.88	3.08	8.56	$1.5\pm^{0.2}_{0.2}$	–	–	A	✗	0.33–0.88	*u*
97	2.73	0.99	133.75	$2.4\pm^{1.0}_{0.9}$	$59\pm^{64}_{36}$	–	C	✗	24–65	*a*
98	3.00	2.38	119.75	$1.7\pm^{0.3}_{0.3}$	$5.84\pm^{5.01}_{3.83}$	–	C	✓	2.0–11	*a*
102	1.57	0.81	12.55	≤4	$43\pm^{44}_{6}$	–	E	✓	4.8–27	*a*
103	2.03	9.41	231.52	$1.8\pm^{0.1}_{0.1}$	$3.35\pm^{0.79}_{0.73}$	–	C	✓	2.6–4.1	*a*
106	0.667	2.33	51.20	1.9†	$30\pm^{8}_{8}$	–	C	✗	6.6–19	*a*
107	0.665	6.05	9.73	$1.6\pm^{0.1}_{0.1}$	$0.77\pm^{0.22}_{0.20}$	–	C	✗	0.57–0.99	*u*
108	2.562	2.99	109.99	$1.7\pm^{0.3}_{0.3}$	$30\pm^{12}_{9}$	–	C	✓	20–42	*a*
109	0.679	3.48	29.01	$2.7\pm^{0.4}_{0.4}$	$71\pm^{34}_{26}$	–	C	✗	40–71	*a*
111	1.097	11.03	72.33	$1.7\pm^{0.2}_{0.2}$	$30\pm^{7}_{7}$	–	E	✗	23–36	*a*
113	0.738	1.69	4.20	$1.9\pm^{0.2}_{0.5}$	$3.60\pm^{2.08}_{1.55}$	–	C	✓	2.8–4.6	*a*
114	1.806	5.54	15.74	≤5	–	–	A	✓	22–120	*a*
116	3.53	4.91	475.68	$1.8\pm^{0.3}_{0.3}$	$43\pm^{16}_{14}$	–	E	✓	22–38	*a*
118	1.609	8.60	172.30	$2.2\pm^{0.1}_{0.1}$	$2.40\pm^{0.27}_{0.25}$	–	C	✓	2.1–2.7	*a*
120	3.591	3.31	217.70	$1.6\pm^{0.1}_{0.1}$	–	–	A	✗	1.3–2.4	*a*
123	1.43	2.93	29.43	$1.7\pm^{0.6}_{0.5}$	$2.34\pm^{2.56}_{1.77}$	–	C	✗	1.8–3.0	*a*
124	0.35	1.39	0.53	$1.8\pm^{0.1}_{0.0}$	–	–	A	✗	≥0.24	–
130	1.628	13.44	212.81	$1.9\pm^{0.0}_{0.0}$	–	–	A	✓	≤0.04	*u*
133	0.671	2.06	3.62	$1.8\pm^{0.1}_{0.1}$	–	–	A	✗	≤0.08	*u*
134	1.609	16.81	224.82	$1.8\pm^{0.0}_{0.1}$	–	–	A	✓	≤0.05	*u*
137	0.751	1.82	6.00	$2.3\pm^{1.1}_{0.8}$	$4.50\pm^{3}_{2}$	$0.067\pm^{0.05}_{0.04}$	D	✗	2.3–5.2	*a*
138	1.220	3.44	23.26	$1.7\pm^{0.1}_{0.1}$	–	–	A	✗	≤0.08	*u*
142	1.38	3.19	19.82	$1.2\pm^{0.5}_{0.4}$	$10\pm^{8}_{5}$	–	C	✗	13–26	*a*
144	3.700	0.93	5592.82	≤4	$249\pm^{89}_{132}$	$0.469\pm^{0.400}_{0.269}$	D	✓	170–350	*a*
146	0.122	8.24	0.33	$1.6\pm^{0.2}_{0.2}$	$1.79\pm^{0.33}_{0.29}$	–	C	✗	1.5–2.1	*a*
147	1.536	5.85	58.53	$1.3\pm^{0.7}_{0.6}$	$59\pm^{42}_{32}$	–	C	✗	27–100	*a*
151	1.51	7.31	74.73	$1.6\pm^{0.1}_{0.1}$	$4.22\pm^{0.92}_{0.82}$	–	C	✓	3.4–5.1	*a*
155	0.732	3.23	6.39	$1.3\pm^{1.0}_{1.0}$	$18\pm^{22}_{15}$	–	C	✗	17–44	*a*
158	2.394	4.54	141.01	$1.6\pm^{0.3}_{0.3}$	$22\pm^{7}_{5}$	–	C	✓	16–30	*a*
161	0.686	7.71	17.00	$1.9\pm^{0.3}_{0.3}$	$7.10\pm^{2.44}_{2.07}$	–	E	✗	5.0–9.5	*a*
165	1.016	4.22	17.69	$1.5\pm^{0.3}_{0.3}$	$6.49\pm^{2.07}_{1.91}$	$0.069\pm^{0.069}_{0.052}$	D	✗	7.0–14	*a*
166	1.36	1.90	36.06	$2.3\pm^{1.7}_{1.0}$	$40\pm^{66}_{25}$	–	C	✗	19–51	*a*
173	1.920	4.78	100.08	$1.8\pm^{0.1}_{0.1}$	–	–	A	✗	≤0.24	*u*
174	1.581	13.85	180.35	$1.8\pm^{0.1}_{0.1}$	–	–	A	✗	≥0.24	–
175	1.52	5.04	57.70	$1.6\pm^{0.4}_{0.3}$	$24\pm^{10}_{7}$	–	C	✓	17–34	*a*
178	1.380	1.24	19.47	$2.3\pm^{0.4}_{0.3}$	$1.11\pm^{0.73}_{0.61}$	–	C	✓	0.92–1.3	–
180	3.064	5.43	376.04	$1.8\pm^{0.4}_{0.3}$	$87\pm^{28}_{23}$	–	C	✓	65–110	*a*
182	1.034	4.96	22.11	$1.7\pm^{0.1}_{0.1}$	–	–	A	✗	≤0.007	*u*
185	0.735	1.65	4.03	$2.0\pm^{0.4}_{0.3}$	$0.59\pm^{0.43}_{0.35}$	–	C	✗	0.49–2.71	–
190	3.10	3.75	204.51	$1.7\pm^{0.2}_{0.1}$	$2.48\pm^{1.72}_{1.55}$	–	C	✗	2.0–3.0	*a*
191	0.821	6.07	14.90	$1.6\pm^{0.1}_{0.1}$	–	–	A	✗	0.04–0.19	*u*
194	2.838	3.64	219.13	$1.9\pm^{0.2}_{0.2}$	$28\pm^{7}_{6}$	–	C	✓	22–35	*a*
197	0.667	1.62	2.48	$1.5\pm^{0.4}_{0.3}$	$0.91\pm^{0.85}_{0.60}$	–	C	✗	0.7–1.1	–
198	0.860	5.82	32.79	$2.2\pm^{0.8}_{0.7}$	$23\pm^{9}_{5}$	–	C	✗	14–24	*a*
200	2.567	10.00	455.99	$1.9\pm^{0.1}_{0.1}$	–	$0.208\pm^{0.140}_{0.093}$	B	✓	≥0.94	–
201	2.713	3.07	164.74	$1.9\pm^{0.1}_{0.1}$	–	–	A	✓	≥0.41	–
203	0.544	78.64	87.31	$1.9\pm^{0.0}_{0.0}$	–	–	A	✓	≥0.24	–
204	0.599	4.11	20.06	$2.7\pm^{0.8}_{0.7}$	$48\pm^{17}_{13}$	–	C	✗	34–65	*a*
210	3.193	1.22	115.02	$2.0\pm^{0.5}_{0.4}$	$7.29\pm^{7.09}_{4.99}$	–	C	✗	2–14	*a*
211	2.612	3.66	122.21	$1.6\pm^{0.2}_{0.2}$	$4.32\pm^{2.34}_{1.97}$	–	C	✓	2.3–6.7	*a*
213	2.202	3.04	35.26	$1.0\pm^{0.2}_{0.2}$	–	–	A	✗	3.8–7.4	*a*
214	1.499	15.36	124.88	$1.2\pm^{0.2}_{0.2}$	$26\pm^{8}_{6}$	$0.362\pm^{0.146}_{0.098}$	D	✗	31–47	*a*
219	2.308	1.68	63.03	$1.9\pm^{0.2}_{0.2}$	–	$0.039\pm^{0.155}_{0.009}$	B	✓	≥0.24	–
221	1.220	2.97	57.61	$2.2\pm^{0.7}_{0.7}$	$86\pm^{36}_{48}$	$0.902\pm^{0.202}_{0.805}$	D	✗	38–79	*a*
222	0.424	2.87	1.93	1.9†	$3\pm^{1}_{1}$	–	C	✗	0.19–0.46	*u*
227	0.834	8.81	30.39	$1.9\pm^{0.4}_{0.5}$	$3.64\pm^{2}_{1}$	$0.400\pm^{0.200}_{0.310}$	D	✗	1.2–1.5	*a*
228	1.216	2.84	21.25	$1.8\pm^{0.2}_{0.2}$	$2.65\pm^{0.93}_{0.79}$	–	C	✓	1.9–3.6	*a*
230	0.520	2.16	2.13	$1.8\pm^{0.3}_{0.3}$	$1.02\pm^{0.49}_{0.49}$	–	C	✗	0.8–1.2	–
231	1.730	2.92	33.05	$1.4\pm^{0.4}_{0.4}$	$14\pm^{8}_{6}$	–	C	✓	7.7–22	*a*
232	1.620	2.58	34.80	$1.8\pm^{0.1}_{0.1}$	–	–	A	✗	≤0.09	*u*
233	1.615	5.67	75.77	$1.7\pm^{0.4}_{0.3}$	$12\pm^{5}_{4}$	$0.116\pm^{0.087}_{0.055}$	D	✓	14–32	*a*
234	0.952	3.11	12.45	$1.8\pm^{0.2}_{0.2}$	$1.04\pm^{0.53}_{0.45}$	–	C	✗	0.91–1.2	–
237	0.620	4.10	6.09	$1.8\pm^{0.1}_{0.1}$	–	–	A	✗	≥0.24	–
244	1.260	4.45	37.87	$1.9\pm^{0.1}_{0.1}$	–	–	A	✗	0.054–0.18	*u*
245	1.864	1.01	6.88	≤1.52	$27\pm^{43}_{17}$	–	C	✗	41–150	*a*
248	0.922	0.77	2.39	$1.5\pm^{0.3}_{0.3}$	–	–	A	✗	0.18–0.53	–
249	0.738	7.35	18.99	$2.1\pm^{0.1}_{0.1}$	–	$0.075\pm^{0.042}_{0.025}$	B	✗	≥0.24	–
262	1.621	8.61	134.48	$1.9\pm^{0.0}_{0.0}$	–	–	A	✓	≤0.04	*u*
265	0.665	3.89	5.80	$1.5\pm^{0.1}_{0.1}$	–	$0.070\pm^{0.080}_{0.030}$	B	✗	0.09–0.18	*u*
269	1.76	4.74	66.75	$1.6\pm^{0.3}_{0.3}$	$2.32\pm^{1.71}_{1.36}$	–	C	✓	1.9–2.8	*a*
273	0.733	4.97	11.38	$1.9\pm^{0.1}_{0.1}$	–	–	A	✗	≤0.008	*u*
277	1.323	6.71	69.56	$2.0\pm^{0.1}_{0.1}$	–	–	A	✗	≤0.06	*u*
281	1.26	8.42	69.26	$1.8\pm^{0.4}_{0.3}$	$0.86\pm^{0.22}_{0.21}$	–	C	✗	0.80–0.92	–
283	2.291	4.46	147.98	$1.8\pm^{0.3}_{0.3}$	$18\pm^{9}_{5}$	–	C	✓	13–24	*a*
284	0.566	4.51	4.80	$1.5\pm^{0.2}_{0.2}$	–	$0.218\pm^{0.038}_{0.048}$	B	✗	–	–
285	2.072	3.58	101.20	$1.9\pm^{0.2}_{0.2}$	–	–	A	✗	≥0.24	–
289	0.607	11.70	12.87	$1.2\pm^{0.2}_{0.2}$	$4.18\pm^{2.56}_{1.74}$	–	E	✗	0.97–1.30	–
291	1.215	3.30	26.54	$1.6\pm^{1.0}_{0.8}$	$39\pm^{30}_{20}$	–	C	✓	28–77	*a*
297	1.44	7.54	118.57	$2.0\pm^{0.6}_{0.5}$	$30\pm^{16}_{11}$	–	C	✓	20–46	*a*
301	0.665	2.25	3.72	$1.7\pm^{0.1}_{0.1}$	–	–	A	✗	0.07–0.20	*u*
305	0.467	28.99	20.75	$1.6\pm^{0.3}_{0.3}$	$0.46\pm^{0.34}_{0.22}$	$0.090\pm^{0.052}_{0.056}$	D	✓	1.2–2.2	*a*
307	0.857	5.53	16.76	$1.7\pm^{0.3}_{0.3}$	$1.06\pm^{0.60}_{0.48}$	–	C	✗	0.9–1.2	–
308	0.736	13.52	30.09	$1.8\pm^{0.0}_{0.0}$	–	–	A	✗	0.01–0.06	*u*
310	0.668	10.21	20.66	$1.9\pm^{0.2}_{0.2}$	$6.93\pm^{1.50}_{1.38}$	–	E	✓	5.6–8.4	*a*
311	2.091	9.34	211.98	$1.7\pm^{0.2}_{0.2}$	$6.36\pm^{1.46}_{1.33}$	–	C	✓	5.1–7.8	*a*
312	1.406	7.44	65.37	$1.6\pm^{0.3}_{0.2}$	$7.38\pm^{3.33}_{2.22}$	–	E	✓	2.0–4.4	*a*
315	0.534	2.83	2.91	$1.8\pm^{0.1}_{0.1}$	–	–	A	✗	≥0.24	–
318	0.663	6.12	11.30	$1.9\pm^{0.2}_{0.2}$	–	$0.186\pm^{0.047}_{0.068}$	B	✗	≥0.24	–
319	0.742	80.80	189.17	$1.9\pm^{0.0}_{0.0}$	–	$0.214\pm^{0.018}_{0.020}$	B	✓	≥0.24	–
320	0.735	3.69	4.64	≤1.87	$9.86\pm^{18.25}_{6.51}$	–	C	✗	17–80	*a*
321	0.733	5.77	8.18	$1.0\pm^{0.1}_{0.1}$	–	–	A	✗	≥0.24	–
323	0.181	2.95	0.25	$1.4\pm^{0.2}_{0.2}$	–	–	A	✗	≤0.03	*u*
324	1.222	2.32	7.63	$0.8\pm^{0.3}_{0.3}$	–	–	A	✓	3–11	*a*
326	1.089	2.80	17.57	1.9†	–	–	C	✓	1.0–1.9	*a*
330	2.208	5.11	132.73	$1.7\pm^{0.1}_{0.1}$	$1.06\pm^{0.80}_{0.74}$	–	C	✗	0.8–1.3	–
337	0.837	25.94	84.93	$1.9\pm^{0.1}_{0.1}$	–	$0.225\pm^{0.022}_{0.026}$	B	✓	≥0.24	–
338	1.27	11.04	55.82	$1.2\pm^{0.2}_{0.2}$	$2.68\pm^{1.74}_{1.32}$	–	C	✓	1.4–4.4	*a*
341	1.324	10.53	144.78	$2.3\pm^{0.0}_{0.0}$	–	–	A	✓	≥0.24	–
344	1.512	18.92	206.39	$1.6\pm^{0.1}_{0.1}$	$10.0\pm^{2}_{2}$	–	E	✗	7.1–9.5	*a*
345	1.235	6.91	69.43	$2.2\pm^{0.1}_{0.1}$	–	–	A	✗	≥0.24	–
358	0.976	68.91	267.86	$1.5\pm^{0.1}_{0.1}$	$12\pm^{2}_{1}$	$0.278\pm^{0.278}_{0.160}$	D	✓	12–14	*a*
359	1.574	34.95	428.02	$1.7\pm^{0.0}_{0.0}$	–	–	A	✓	≥0.24	–
361	0.977	20.00	89.39	$1.9\pm^{0.0}_{0.0}$	–	–	A	✓	≥0.24	–
366	2.34	3.27	73.65	$1.5\pm^{0.2}_{0.2}$	–	–	A	✓	1.8–3.1	*a*
374	1.041	13.20	58.81	$1.5\pm^{0.3}_{0.3}$	$13\pm^{5}_{3}$	–	C	✗	9–18	*a*
375	1.350	4.34	49.77	$2.1\pm^{0.1}_{0.1}$	–	$0.063\pm^{0.052}_{0.087}$	B	✓	–	–
382	0.527	46.04	50.58	$1.7\pm^{0.1}_{0.1}$	$4\pm^{3}_{4}$	$0.398\pm^{0.083}_{0.080}$	D	✗	0.18–0.28	*u*
385	1.220	7.46	36.03	$1.3\pm^{0.3}_{0.2}$	$2.70\pm^{1.59}_{1.23}$	–	C	✗	1.5–4.3	*a*
388	0.605	4.24	5.44	$1.6\pm^{0.1}_{0.2}$	–	–	A	✗	≥0.24	–
390	1.118	6.30	41.36	$1.9\pm^{0.1}_{0.1}$	–	–	A	✗	≥0.24	–

Notes. Column (1) is the identification number of X-ray sources listed in Ranalli et al. (in prep.); Col. (2) is the redshift of the source (rounded to two (photometric) or three (spectroscopic) decimal); Col. (3) gives the observed 2–10 keV flux of the source in units of 10^{-15} erg/s/cm^2; Col. (4) gives the unabsorbed rest-frame 2–10 keV luminosity of the source using the best fit model in units of 10^{42} erg/s; Col. (5) is the X-ray photon index, Γ, where † indicates that the index was frozen in the fit; Col. (6) is the intrinsic column density N_H measured from the best fit model in Col. (8) in units 10^{22} cm^{-2}; Col. (7) gives the electron temperature for the soft Comptonisation component in units of keV; Col. (8) is the best-fitting model for the spectrum as described in Sect. 3.1, see also Table 3; Col. (9) is a tick to denote whether the sources is classified as IR power-law or IR no-power-law galaxy; (10) 1σ confidence interval on the intrinsic column density N_H^{intr} measured using models C, D, E in units of 10^{22} cm^{-2} (see Sect. 5); (11) classification of the source as absorbed, unabsorbed and unclassified as *a*, *u* and –, respectively (see Sect. 5).

Table 2. Summary of the mean value of the general X-ray properties given by the best fitted model (see Sect. 3).

X-ray parameter	Sample	IR pl	IR no-pl	KS
$\langle\Gamma\rangle$	1.72 ± 0.36	1.74 ± 0.36	1.71 ± 0.37	∼65%
$\langle\log(N_{\rm H}^{\rm intr})\rangle$	22.00 ± 1.81	22.13 ± 1.36	21.89 ± 1.34	≲10%
$\langle z\rangle$	1.42 ± 0.81	1.81 ± 0.79	1.15 ± 0.70	–
$\langle\log(F_{2-10\,\rm keV})\rangle$	−14.35 ± 0.63	−14.33 ± 0.91	−14.36 ± 0.32	∼30%
$\langle\log(L_{2-10\,\rm keV})\rangle$	43.50 ± 0.84	43.80 ± 0.99	43.28 ± 0.63	≲3%

Notes. The last column is the probability that both distributions (IR power-law and IR non-power-law sample) come from the same distribution according to the Kolmogorov-Smirnov test.

Table 3. Summary of the results of the spectral fitting.

Model	N		$N_{\rm IRpl}$		$N_{\rm IRnon-pl}$	
(1)	(2)		(3)		(4)	
A: *powerlaw*	45	$(31\pm^{6}_{6})$	15	$(25\pm^{10}_{8})$	30	$(34\pm^{9}_{8})$
B: *zbbody + powerlaw*	13	$(9\pm^{4}_{3})$	9	$(15\pm^{8}_{6})$	4	$(5\pm^{4}_{3})$
C: *zphabs × powerlaw*	69	$(47\pm^{7}_{7})$	27	$(45\pm^{10}_{-10})$	42	$(48\pm^{9}_{8})$
D: *zbbody + (zphabs × powerlaw)*	12	$(8\pm^{4}_{3})$	5	$(8\pm^{7}_{5})$	7	$(8\pm^{6}_{4})$
E: *powerlaw + (zphabs × powerlaw)*	8	$(5\pm^{4}_{3})$	4	$(6\pm^{7}_{4})$	4	$(5\pm^{4}_{3})$

Notes. (1) XSPEC model definition: *power-law* as a simple photon power-law; *zphabs* as a rest-frame photoelectric absorption; *zbbody* as a redshifted blackbody spectrum. All models include Galactic absorption (*phabs*). (2) Total number and fraction of best fitted AGN with the indicated model. (3) Number and fraction of IR *power-law objects* best fitted with the indicated model. (4) Number and fraction of IR *non-power-law objects* best fitted with the indicated model.

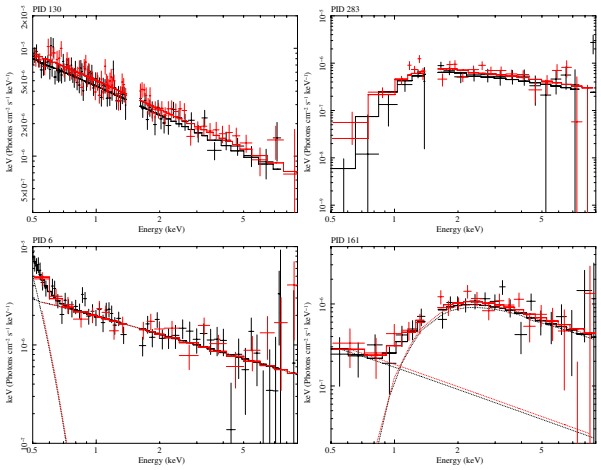

Fig. 3. Example X-ray spectra of four objects whose best-fit model is a simple power law (model A), absorbed power law (model C), a simple power law with thermal soft excess (model B) and an absorbed power law with a Thomson scattering component (model E), respectively (ID210 = 130, ID210 = 283, ID210 = 6, ID210 = 161).

(see Fig. 1), for which the soft component is often shifted below the used X-ray spectral band.

– *Compton-Thick candidates*.
The simple power-law model gives a good fit for 58 (39^{+6}_{-7}%) X-ray sources, i.e. A and B models. The remaining 89 (61^{+6}_{-7}%) sources display a best fit with X-ray obscuration, i.e., C, D, and E models. The intrinsic absorption distribution measured is bimodal (see Fig. 4), in the sense that 39^{+7}_{-6}% of sources have very small $N_{\rm H}^{\rm intr}$ (below the Galactic value) and appear separated from the distribution of the bulk of the sources. The lowest bin in the distribution (i.e., that with $N_{\rm H}^{\rm intr} \simeq 10^{20}$ cm^{-2}) accumulates those sources for which we cannot measure any intrinsic absorption, i.e. it includes all the sources best fitted with an unabsorbed model (model A and B, see Table 3). The last bin at $N_{\rm H}^{\rm intr} = 10^{24}$ cm^{-2} includes the few sources with $N_{\rm H}^{\rm intr} > 10^{24}$ cm^{-2} but their error bars make them compatible with being *Compton-Thin*. Thus, there are no *Compton-Thick* sources securely detected in our sample using the first-order spectral model adopted in this paper (see Table 4 and further discussion below). In Fig. 4, we also show the normalised distribution of the intrinsic absorption for the sample by Tozzi et al. (2006). The excess of sources in the lowest bin of our sample can be explained through the lack of sources with detected intrinsic absorption to $N_{\rm H}^{\rm intr} \sim 10^{21-22}$ cm^{-2}, as we are really not sensitive for most of our sources to intrinsic column densities to $N_{\rm H}^{\rm intr} \sim 10^{21-22}$ cm^{-2}, especially at high redshifts. We remark that both distributions have in general a similar shape but they differ at large absorptions (see Fig. 4, bottom left panel), in the Compton-Thick region.

In summary, 69 objects appear to be unabsorbed X-ray sources, i.e., their best-fit X-ray absorption column is $N_{\rm H}^{\rm intr} < 10^{22}$ cm^{-2}. That is, 78 (53^{+7}_{-7}%) of the galaxies in our sample host significantly obscured active nuclei what is not far but still on the lower side from that predicted by XRB synthesis models (∼64%, Gilli et al. 2007). 60 (77^{+16}_{-11}%) of 78 are Compton-Thin with a moderate obscuration ($N_{\rm H}^{\rm intr} \leq 3 \times 10^{23}$ cm^{-2}) and the remaining 18 objects are heavily obscured AGN. Among these, we find two Compton-Thick candidates in the sample (right-most bin in the bottom panel in Fig. 4), in the sense that the column density has some likelihood of exceeding 1.5×10^{24} cm^{-2}. However, the uncertainty in the intrinsic column densities of these sources (ID210 = 66 IR non-power-law, and ID210 = 144 IR power-law), is such that their Compton-Thin nature cannot be ruled out. If additional criteria are introduced this dichotomy

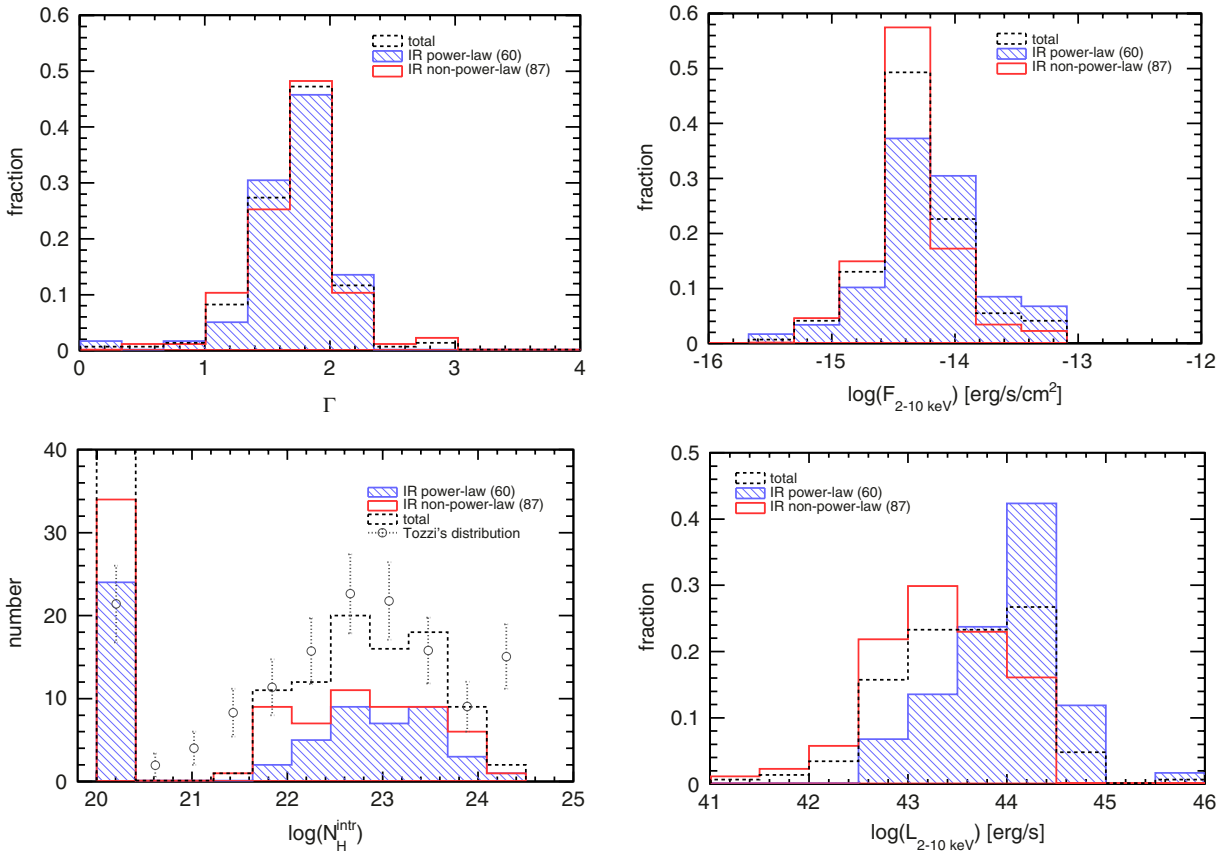

Fig. 4. *Top panels*: normalised distribution of the X-ray power-law photon index and the observed 2–10 keV flux. *Bottom panels*: normalised distribution of the intrinsic absorption and the rest-frame 2–10 keV luminosity corrected for both Galactic and intrinsic absorption. The error points in the intrinsic absorption distribution show the $N_{\rm H}^{\rm intr}$ distribution for the sample given by Tozzi et al. (2006). Solid-line shaded and empty histograms show the distribution for the IR power-law and IR no power-law populations, respectively. The dashed-line empty histogram shows the distribution for the entire sample. All the values are given by the best fitted model (see Sect. 3).

Table 4. Summary of the sources in our sample that were identified as Compton-Thick candidates (CThick) in other works.

ID210	us	T06	C11	B12	I12	G13
30	heavily	–	–	–	heavily	–
44	unabsorbed	CThick	–	heavily	–	–
48	moderately	–	–	–	–	heavily
64	heavily	–	–	–	heavily	–
66	heavily	–	–	–	–	secure-CThick
106	moderately	CThick	–	heavily	–	–
114	heavily	–	–	–	heavily	–
144	heavily	CThick	CThick	heavily	heavily	secure-CThick
147	heavily	CThick	CThick	heavily	–	secure-CThick
155	moderately	CThick	–	heavily	–	–
180	heavily	–	–	–	heavily	heavily
214	heavily	–	–	–	–	heavily
222	unabsorbed	–	–	–	–	heavily
245	heavily	–	–	–	heavily	heavily
289	moderately	–	–	–	–	heavily
324	unabsorbed	–	–	–	–	secure-CThick

Notes. *us*: this work; *T06*: Tozzi et al. (2006); *C11*: Comastri et al. (2011); *B12*: Brightman & Ueda (2012); *I12*: Iwasawa et al. (2012); and *G13*: Georgantopoulos et al. (2013).

could be resolved and more sources could be identified as Compton-Thick.

For example, we find that our best-fit value of the column density to sources ID210 = 144, 147 using an absorbed power-law model is in very good agreement with the fit to the *XMM-Newton* spectrum of the same sources with the more sophisticated torus model of Murphy & Yaqoob (2009) by Comastri et al. (2011) using the same ultra-deep *XMM-Newton* data in the CDFS. The uncertainties on the fitted column density do not allow us to assert that they are

Compton-Thick, but Comastri et al. (2011) use the presence of a strong Iron line and a strong reflection component to classify source ID210 = 147 as such.

Similarly, Georgantopoulos et al. (2013) have conducted a search for Compton-Thick AGN using the same *XMM-Newton* exposures. The spectral model that they fitted to the data is PLCABS (Yaqoob 1997), which is specially tailored to Compton-Thick sources, as it properly takes Compton scattering and reflection up to column densities up to $\sim 5 \times 10^{24}$ cm^{-2} into account. A total of 9 candidate Compton-Thick sources (numbers ID210 = 48, 66, 144, 147, 214, 222, 245, 289 and 324) were found by them. Our analysis of the X-ray spectra of these 9 sources is coincident with theirs in terms of best-fit spectral index and absorbing column. They classify four of these (ID210 = 144, 66, 147, 324) as Compton-Thick: the first two had transmission-dominated spectra with strong Iron lines (we also find them to be heavily absorbed) and the last two because of their reflection-dominated spectra (we also detect 66 as a strongly absorbed source, but not 324, because in our fit a flat unabsorbed model mimics its intrinsic reflection-dominated spectrum).

Another paper using the same *XMM-Newton* exposures dealing with obscured AGN is Iwasawa et al. (2012), who label sources ID210 = 30, 64, 144, 180, 245, 114 as strongly absorbed sources in agreement with our findings. Again, the last source was found by them to be a possible Compton-Thick candidate because of its reflection-dominated spectrum, while our best-fit model is a flat spectrum with a moderate column density.

Other works to characterize obscuration using deep X-ray data in the same region of the sky have also been carried out by Tozzi et al. (2006) and Brightman & Ueda (2012). The sources ID210 = 44, 106, 155, 144, and 147 were identified as Compton-Thick sources by Tozzi et al. (2006) with their 1 Ms *Chandra* data. We disagree with the Compton-Thick character of ID210 = 44, 106, and 155, which appear to be at most moderately absorbed in our analysis, while the last two would be heavily absorbed, in agreement with Brightman & Ueda (2012), but see the discussion above about those last two sources using additional criteria.

While all models predict that Compton-Thick sources have an important role to play in filling the so far unresolved XRB above ~8 keV, such sources have been generally elusive in X-ray surveys conducted both with *Chandra* and *XMM-Newton*. This is also evidenced in the current work, which shows that even with the deepest exposures it is very difficult to unambiguously find sources with column densities in excess of 10^{24} cm^{-2}. In the case of our *XMM-Newton* data this is likely due to a combination of large background at high energies together with a modest (but still significant) effective area. In the case of *Chandra* data, a much more reduced background (since the better angular resolution enables a much smaller extraction region for the X-ray spectra) is hardly compensated by a smaller effective area with respect to *XMM-Newton*. Detecting significant numbers of Compton-Thick sources remains a challenge with current X-ray instruments.

– *IR power-law versus IR non-power-law from best-fit model.* On the one hand, we found that both the measured X-ray photon index and the observed X-ray flux remain virtually confined to the mean value of $\langle\Gamma\rangle = 1.72 \pm 0.36$ and $\langle\log(F_{2-10\,\mathrm{keV}})\rangle = -14.35 \pm 0.63$ erg/s/cm^2, respectively. There is one unabsorbed AGN (ID210 = 114 IR power-law) for which the resulting photon index is >3. This very steep slope is probably a consequence of both the small number of counts and high background in its X-ray spectrum, although we cannot exclude a very high accretion rate source, e.g., a Narrow-Line Seyfert 1 galaxy.

On the other hand, the distribution of the intrinsic absorption and the rest-frame 2–10 keV luminosity appears to span distinct regions (see Sect. 5). There are some evidence that the distribution of the intrinsic absorption column densities seems to have a different shape for IR power-law and IR non-power-law populations according to the Kolmogorov-Smirnov test ($\lesssim$10%), which suggests that both samples might have different parent distributions. Finally, we also found that the rest-frame 2–10 keV luminosity distribution appears to have a different shape for IR power-law and IR non-power-law populations according to the Kolmogorov-Smirnov test ($\lesssim$3%). The mean values for the logarithmic X-ray luminosity are 43.8 ± 0.99 and 43.28 ± 0.63 for the IR power-law and IR non-power-law populations, respectively. The IR power-law population appears to select better higher luminosity AGN because as expected, the IRAC selection cannot efficiently identify low-luminosity AGN, and appears to be incomplete for low luminosity AGN (see Donley et al. 2007, 2008).

5. Intrinsic absorption

To explore and quantify the efficiency in finding highly-obscured AGN and/or QSO when selecting the sources as IR power-law and IR non-power-law, all individual spectra were re-fitted by an absorbed power-law model (plus a soft-excess component when required by the X-ray data), i.e., using models `C`, `D` or `E`. In addition, now, for those sources with a small number of counts (<500), the X-ray power-law photon index (Γ) was fixed to 1.9 (the typical average value for unabsorbed AGN) to constrain better the intrinsic absorption. As expected, for the sources, which had already been fitted with models `C`, `D`, or `E` the results remain essentially unchanged, the only difference is that now we assign a 1σ uncertainty interval to the intrinsic column density. Similarly, for the sources whose best-fit model was `A` or `B` the results are essentially compatible except for 8 sources, which are now classified as absorbed. This happens because of two reasons: on two cases, the photon index is now fixed to 1.9, because of the low number of counts, hence the fitted absorption increased considerably because these sources had low values of the photon index; on the other six sources, the F-test probability of models `C`, `D`, `E` versus `A`, `B` was $\gtrsim$90% (hence the former were not significantly better than the latter, according to our criterion in Sect. 3: the 95% confidence interval on $N_{\mathrm{H}}^{\mathrm{intr}}$ includes zero) while the bottom of the 1σ confidence interval on $N_{\mathrm{H}}^{\mathrm{intr}}$ is above 10×22 cm^{-2} (i.e., they are absorbed according to our classification in this section). The intrinsic hard X-ray luminosities derived in this section and in Sect. 3 are very similar, solely in two cases the ratio between both luminosities exceeds a factor 1.5, but in all cases the source remains in the same luminosity bin (defined below).

– *Absorbed fraction from best-fit values.* We have subdivided our IR power-law and IR non-power-law samples according to their $N_{\mathrm{H}}^{\mathrm{intr}}$ values, also taking the 1σ uncertainty intervals into account, in the sense that those sources whose 1σ uncertainty interval is fully above (below) 10^{22} cm^{-2} are called absorbed (unabsorbed) at the 1σ level. Those objects whose 1σ interval crosses the 10^{22} cm^{-2} border have been labelled as *unclassified*. The number of

Table 5. Number of sources classified as absorbed/unabsorbed (at 1σ significance) and unclassified as a function of the intrinsic 2–10 keV luminosity according to their intrinsic column density.

Sample	Absorbed				Unclassified				Unabsorbed				Total
	$\log L_X$ [erg/s]				$\log L_X$ [erg/s]				$\log L_X$ [erg/s]				
	<43	43–44	≥44	all	<43	43–44	≥44	all	<43	43–44	≥44	all	
IR power-law	5	15	21	41	0	6	7	13	1	0	5	6	60
IR non-power-law	5	28	9	42	10	10	4	24	10	10	1	21	87
Ttotal	10	43	30	83	10	16	11	37	11	10	6	27	147

Notes. The N_H^{intr} is obtained assuming an absorbed power-law model (i.e., `C`, `D`, and `E` model). We remark that absorbed/unabsorbed and unclassified groups are disjoint sets.

sources in each of these subdivisions in bins of 2–10 keV luminosity is listed in Table 5 and the individual classification of each source is shown in Table 1. As a further test of the robustness of our estimates, we also redefined the absorbed and unabsorbed samples using a 2σ threshold around 10^{22} cm^{-2}. The number of sources in each subsample change very little, and our conclusions remain unaffected. In what follows, in our conservative approach those sources whose were classified as *unclassified* will be considered as unabsorbed.

We measured a significant intrinsic absorption in excess of 10^{22} cm^{-2} for 83 sources (see Table 1), of which 41 are IR power-law and 42 are IR non-power-law AGN. A further 27 galaxies are classified as unabsorbed, out of which 6 are IR power-law and 24 IR non-power-law galaxies. 37 sources were unclassified at 1σ level.

An important result from this work is that the fraction of absorbed sources (see Table 5) is higher among the IR power-law galaxies (41 out of 60) than among the IR non-power-law galaxies (42 out of 87). Binomial error estimates return a fraction of absorbed sources among the IR power-law galaxies of 68^{+9}_{-10}% and of 48^{+9}_{-8}% for the IR non-power-law galaxies. A Bayesian estimate of the probability of these two fractions coming from the same parent distribution (Stevens et al. 2005) yields a probability of 0.0023, and therefore the fraction of absorbed sources among IR power-law galaxies is higher than that of IR non-power-law galaxies at about the 3σ level.

– *Dependence on X-ray luminosity from best-fit values.*
Our next step was to check for a possible dependence of the column density on luminosity, within the two subsamples. We selected three luminosity ranges, $\leq 10^{43}$ erg s^{-1}, 10^{43}–10^{44} erg s^{-1}, and $>10^{44}$ erg s^{-1} with median redshifts of 0.65 ± 0.11, 1.59 ± 0.69, and 2.21 ± 0.75, respectively. We compute the fraction of IR power-law (IR non-power-law) sources, which have been classified as *absorbed* AGN at each luminosity range, understood as the ratio of the number of absorbed IR power-law (IR non-powerlaw) at 1σ level to the total number of IR power-law (IR non-powerlaw) sources at this luminosity bin. We found that the fraction of absorbed sources appears roughly constant with luminosity for the IR power-law AGN, while it grows from ∼20% to ∼64% for the IR non-power-law galaxies (see Fig. 5).

– *Dependence on X-ray luminosity from probability density functions.*
To take the full distribution of probabilities when building the N_H^{intr} distributions into account, we followed the following procedure. First, when fitting the X-ray spectrum of each individual source, we used the `steppar` command under the `XSPEC` fitting package, to find out how the χ^2 varies with $\log(N_H^{intr})$. We explored sufficiently wide ranges of $\log(N_H^{intr})$ in such a way that $\Delta\chi^2 = \chi^2 - \chi^2_{min}$ (where χ^2_{min} corresponds to the best-fit N_H^{intr} value) reaches sufficiently high values (hence low probabilities, see below). We set an absolute minimum of $\log(N_H^{int}) = 20.0$, because, as discussed before, our data are not sensitive to lower values of the intrinsic absorption. Next, we constructed a probability density function for N_H^{intr} of each individual source by using $p(\log(N_H^{intr})) \propto \exp(-\Delta\chi^2/2)$, and normalised it between $\log(N_H^{int}/\mathrm{cm}^{-2}) = 20$ and 25. We registered these $p(\log(N_H^{intr}))$ into a common grid of values of $\log(N_H^{intr})$ spaced 0.2 units. of X-ray luminosities and for the full sample, also taking both IR power-law and IR non-power-law populations into account, normalising each of the summed probabilities to a total unit area (see Fig. 6).

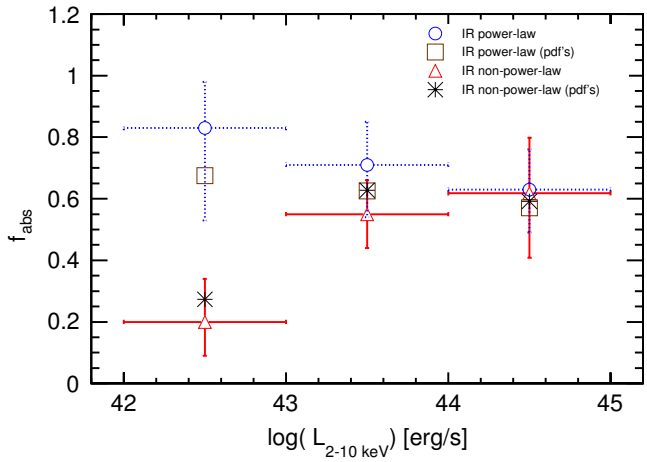

Fig. 5. Fraction of absorbed sources (at $\geq 1\sigma$) for IR power-law and IR non-power-law galaxies as a function of the rest-frame absorption corrected 2–10 keV luminosity. The open squares and star symbols show the fraction of absorbed sources taking into account the probability density function for N_H^{intr} of each individual source for IR power-law and IR non-power-law, respectively (see Sect. 5). Note that these fractions refer exclusively to our sample and not to the overall AGN population.

The normalised distributions of N_H^{intr} for the entire sample show some difference between the two populations of IR power-law and IR non-power-law galaxies, with the former being more heavily absorbed than the latter. This behaviour is not evident at high or intermediate luminosities, where both populations have an overall indistinguishable distribution. However, at the lowest luminosity regime, the distributions appear to have a quite different shape. Whilst the N_H^{intr} distribution for the IR power-law sample peaks at $\sim 10^{23}$ cm^{-2}, the IR non-power-law sample appears to have largely unabsorbed sources. This is somewhat unexpected because of the known incompleteness of the power-law

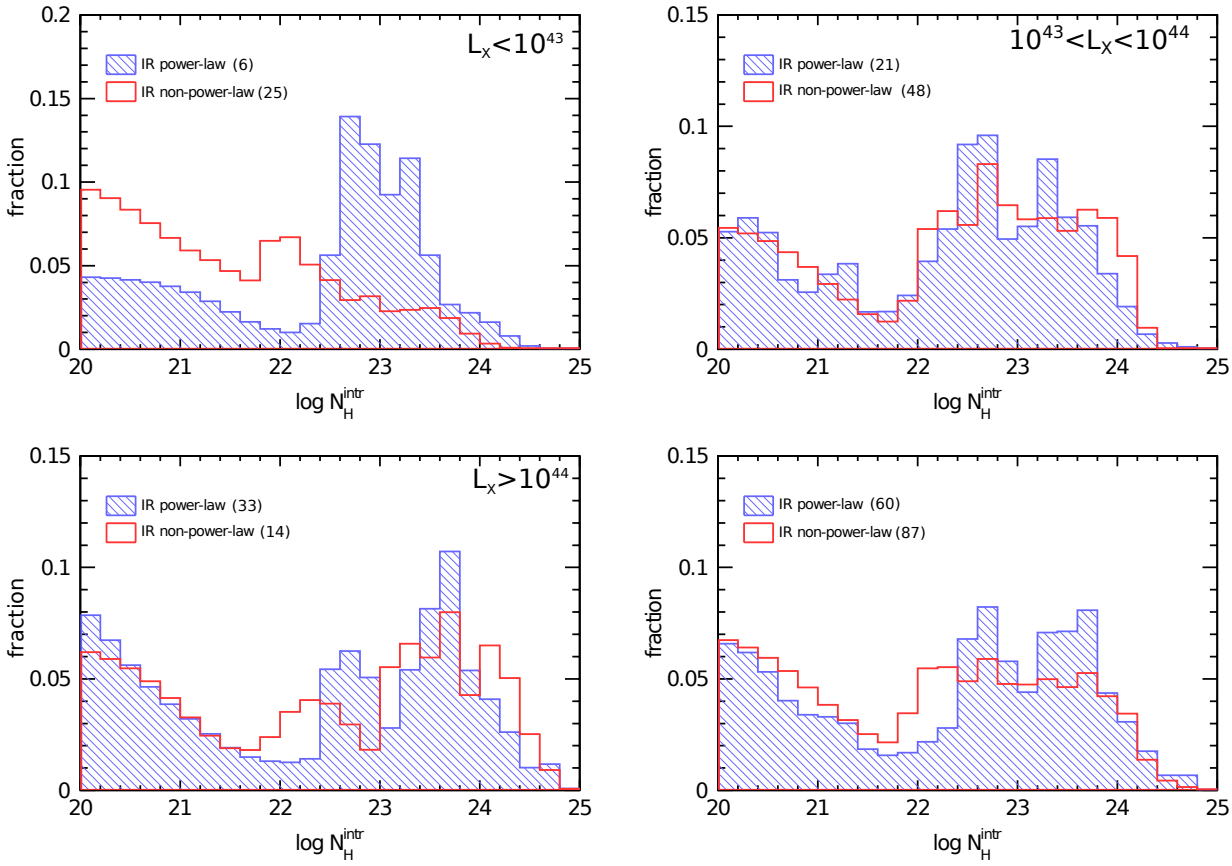

Fig. 6. Normalised distribution of intrinsic absorbing column densities (in log units) in three absorption corrected 2–10 keV luminosity bins (*upper panels* and *lower left panel*) and for the entire sample (*lower right panel*). The distributions were computed using the probability density function for N_H^{intr} of each individual source (see Sect. 5, for details).

selection at low AGN luminosities. We interpret this as due to the different shapes of the IR AGN SEDs of type-1 and type-2, with type-2 having steeper SEDs (see Ramos Almeida et al. 2011, Fig. 9). The host galaxy, on the other hand, has a "broad" bump peaking at ∼1.6 μm (rest-frame). Therefore, the combination of a relatively low luminosity type-1 AGN and its host galaxy would result in a relatively flat spectral shape in the IRAC bands, likely not meeting the IRAC IR power-law criteria.

As a further test of the robustness of our estimates, we also measured the fraction of absorbed sources in both samples at each luminosity bin using the probability density function for N_H^{intr} of each individual source. The absorbed source fractions change very little (see Fig. 5) both results being compatible. Moreover, if we compute the absorbed source fraction without those sources with photometric redshift (11/60 IR power-law and 12/87 IR non-power-law sources), our findings are also in good agreement when accounting for uncertainties.

Therefore, taking the full probability distribution of $\log(N_H^{intr})$ into account, our analysis is in full agreement with the one using just the 1σ confidence levels: the fraction of absorbed sources among IR-power-law AGN is higher both in the full sample and among lower luminosity sources ($\log L_X < 43$ erg/s), while it is compatible with being similar at higher luminosities. We note that, on the one hand, we are not trying to determine the absolute fraction of absorbed sources as a function of the X-ray luminosity, but to evaluate the effectiveness of the mid-IR selection to identify obscured AGN by comparing the fraction of absorbed sources inside and outside the IRAC-selection wedge. On the other hand, we do not apply any completeness correction to the absorbed source fractions, thus these fractions of absorbed sources should not be compared with results referring to the overall AGN population (Ueda et al. 2003; Treister & Urry 2005; Gilli et al. 2007). We also point out that the difference on the fraction of obscured AGN at the lowest luminosity bin should be interpreted with caution, since there are only 6 IR power-law sources in this low-luminosity bin.

In conclusion, although the IR power-law selection only picks up 60/147 (about 41%) of our X-ray-selected high-spectral-quality sources, at high X-ray luminosities it singles out about 70% of our sources (33/47). Concentrating on the IR power-law sources, the overall percentage of such sources, which are absorbed is 68% (41/60), essentially independent of the AGN luminosity, better than the overall fraction of absorbed sources in our full sample (83/147 ∼ 56%) and significantly higher than that of IR non-power-law sources (42/87 ∼ 48%). As Donley et al. (2012) found, the IR power-law selection produces an incomplete census of AGN, its completeness being a strong function of AGN luminosity. Our overall estimate of its efficiency to find absorbed sources (∼70%) is similar, if somewhat lower, than their estimate of ∼75%.

6. Summary and conclusions

In the paper we have investigated the subset of X-ray sources in the ultra-deep *XMM-Newton* of the *Chandra* Deep Field South (Ranalli et al. 2013) with a highly significant (>8σ) detection,

high exposure time (>1 Ms) and known (spectroscopic or photometric) redshift, totalling 147 sources. All of them turn out to have *Spitzer*/IRAC counterparts, and they are all detected in the four IRAC bands. Consequently, our final sample is biased towards high signal-to-noise X-ray sources and cannot be considered as a complete sample of X-ray selected or mid-IR-selected sample. However, this does not affect the work main goal of this: to test the efficiency of the IR power-law in selecting absorbed X-ray sources. We have used the IRAC photometry to classify these sources into IR power-law and IR non-power-law galaxies, according to whether or not their IR SED has a power-law-like shape and is monotonically increasing, following Donley et al. (2012).

We have estimated the absorbing column density assuming an absorbed power-law model. Each source was classified as absorbed, or unabsorbed at 1σ level, in the sense that those sources whose 1σ uncertainty interval is fully above 10^{22} cm^{-2} or not (respectively). And finally, we further explore possible mismatches in the observed X-ray absorption distributions for these subsamples (IR power-law and IR non-power-law) at three intrinsic rest-frame 2–10 keV luminosity bins ($<10^{43}$ erg/s, 10^{43-44} erg/s, and $>10^{44}$ erg/s). The goal was to investigate whether the IR power-law criteria selects more absorbed AGN or not, and specifically whether it is effective at selecting type-2 AGN at a given luminosity range. The main results from our work are as follows:

- All high-X-ray-spectral-quality sources in the deepest *XMM-Newton* field have counterparts in the *Spitzer*/IRAC bands, therefore using mid-IR data to search for obscured sources does not leave out any candidates.
- With our absorbed-power-law X-ray spectral analysis, 21 out of 147 sources are heavily absorbed ($N_{\rm H}^{\rm intr} > 3\times10^{23}$ cm^{-2}) but, when taking the uncertainties into account, we cannot confirm the Compton-Thick nature of any of our sources. We are, however, in full agreement with other papers using the same deep *XMM-Newton* data, which use additional criteria to that end.
- At more than 3σ level, we find that the fraction of absorbed sources among the IR power-law populations (68^{-9}_{+8}%) appears significantly higher than that for IR non-power-law galaxies (48^{-10}_{+9}%).
- We also found that the fraction of absorbed sources appears roughly constant (~70) with luminosity for the IR power-law AGN, while it grows from ~20% to ~65% for the IR non-power-law galaxies with increasing luminosity.
- The main difference in the absorbed fraction between the IR power-law and the IR non-power-law sources happens at the lowest X-ray luminosities ($<10^{43}$ erg/s). We understand this in terms of contrast with the host galaxy, in the sense that type-2 AGN (in principle absorbed in X-rays) are more easily picked up by those criteria than type-1 AGN (unabsorbed) at low luminosities.

We conclude that the Donley et al. (2012) IR power-law criteria, if admittedly incomplete, favour the selection of absorbed sources among the X-ray detected AGN. This is particularly clear at low X-ray luminosities. This prompts the question about the nature of the IR power-law sources in the *XMM-Newton* area without X-ray detection. Since we do not miss any X-ray-detected sources by using mid-IR data and about 2/3 of the selected sources turn out to be absorbed, it is likely that the mid-IR power-law criteria would pinpoint absorbed AGN among X-ray undetected sources. These sources would still be detected in the mid-IR (from the reprocessing of the AGN radiation), but they would have high absorbing column densities, placing them beyond the current capabilities of our most powerful observatories pushed to their limit.

Acknowledgements. We are grateful to the referee for comments that helped improve the paper. This work is based on observations obtained with *XMM-Newton*, an ESA science mission with instruments and contributions directly funded by ESA Member States and NASA. N.C.-M., F.J.C., S.M. and X.B. acknowledge financial support provided by the Spanish Ministry of Economy and Competitiveness through grant AYA2010-21490-C02-01. S.M., F.J.C. and A.A.-H. acknowledge financial support by the Spanish Ministry of Economy and Competitiveness through grants AYA2010-21490-C02-01 and AYA2012-31447. SM acknowledges financial support from the JAE-Doc program (Consejo Superior de Investigaciones Cientficas, cofunded by FSE). A.A.-H. acknowledges support from the Universidad de Cantabria through the Augusto G. Linares program. P.G.P.-G. acknowledges support from the Spanish Programa Nacional de Astronomía y Astrofísica under grants AYA2009-07723-E and AYA2009-10368. This work has made use of the Rainbow Cosmological Surveys Database, which is operated by the Universidad Complutense de Madrid (UCM). We acknowledge financial contribution from the agreement ASI-INAF I/009/10/0 and from the INAF-PRIN-2011.

References

Alonso-Herrero, A., Ward, M. J., & Kotilainen, J. K. 1996, MNRAS, 278, 902
Alonso-Herrero, A., Pérez-González, P. G., Alexander, D. M., et al. 2006, ApJ, 640, 167
Antonucci, R. 1993, ARA&A, 31, 473
Arnaud, K. A. 1996, in Astronomical Data Analysis Software and Systems V, eds. G. H. Jacoby, & J. Barnes, ASP Conf. Ser., 101, 17
Assef, R. J., Stern, D., Kochanek, C. S., et al. 2013, ApJ, 772, 26
Avni, Y. 1976, ApJ, 210, 642
Barger, A. J., Cowie, L. L., Mushotzky, R. F., et al. 2005, AJ, 129, 578
Barvainis, R. 1987, ApJ, 320, 537
Bauer, F. E., Alexander, D. M., Brandt, W. N., et al. 2004, AJ, 128, 2048
Brandt, W. N., & Hasinger, G. 2005, ARA&A, 43, 827
Brightman, M., & Ueda, Y. 2012, MNRAS, 423, 702
Caccianiga, A., Severgnini, P., Braito, V., et al. 2004, A&A, 416, 901
Comastri, A., & the XMM-CDFS team 2013 [arXiv:1304.3664]
Comastri, A., Fiore, F., Vignali, C., et al. 2001, MNRAS, 327, 781
Comastri, A., Ranalli, P., Iwasawa, K., et al. 2011, A&A, 526, L9
Della Ceca, R., Caccianiga, A., Severgnini, P., & et al. 2008, A&A, 487, 119
Dickey, J. M., & Lockman, F. J. 1990, ARA&A, 28, 215
Donley, J. L., Rieke, G. H., Pérez-González, P. G., et al. 2007, ApJ, 660, 167
Donley, J. L., Rieke, G. H., Pérez-González, P. G., et al. 2008, ApJ, 687, 111
Donley, J. L., Koekemoer, A. M., Brusa, M., et al. 2012, ApJ, 748, 142
Edelson, R. A., & Malkan, M. A. 1986, ApJ, 308, 59
Elvis, M., Wilkes, B. J., McDowell, J. C., et al. 1994, ApJS, 95, 1
Fabian, A. C. 1999, MNRAS, 308, L39
Fazio, G. G., Hora, J. L., Allen, et al. 2004, ApJS, 154, 10
Feruglio, C., Daddi, E., Fiore, F., et al. 2011, ApJ, 729, L4
Franceschini, A., Manners, J., Polletta, M. d. C., et al. 2005, AJ, 129, 2074
Galbiati, E., Caccianiga, A., Maccacaro, T., el al. 2005, A&A, 430, 927
Georgantopoulos, I., Georgakakis, A., & Akylas, A. 2007, A&A, 466, 823
Georgantopoulos, I., Akylas, A., Georgakakis, A., et al. 2009, A&A, 507, 747
Georgantopoulos, I., Comastri, A., Vignali, C., et al. 2013, A&A, 555, A43
Gilli, R., Salvati, M., & Hasinger, G. 2001, A&A, 366, 407
Gilli, R., Comastri, A., & Hasinger, G. 2007, A&A, 463, 79
Granato, G. L., & Danese, L. 1994, MNRAS, 268, 235
Helou, G., Roussel, H., Appleton, P., et al. 2004, ApJS, 154, 253
Hickox, R. C., & Markevitch, M. 2006, ApJ, 645, 95
Iwasawa, K., Gilli, R., Vignali, C., et al. 2012, A&A, 546, A84
King, A. 2005, ApJ, 635, L121
Komatsu, E., Dunkley, J., Nolta, M. R., et al. 2009, ApJS, 180, 330
Kotilainen, J. K., Ward, M. J., Boisson, C., et al. 1992, MNRAS, 256, 125
Lacy, M., Storrie-Lombardi, L. J., Sajina, A., et al. 2004, ApJS, 154, 166
Lehmer, B. D., Brandt, W. N., Alexander, D. M., et al. 2005, ApJS, 161, 21
Lu, N., Helou, G., Werner, M. W., et al. 2003, ApJ, 588, 199
Luo, B., Brandt, W. N., Xue, Y. Q., et al. 2011, ApJ, 740, 37
Magnelli, B., Chary, R. R., Pope, A., et al. 2008, ApJ, 681, 258
Maiolino, R., & Rieke, G. H. 1995, ApJ, 454, 95
Mateos, S., Barcons, X., Carrera, F. J., et al. 2005, A&A, 444, 79
Mateos, S., Saxton, R. D., Read, A. M., et al. 2009, A&A, 496, 879
Mateos, S., Carrera, F. J., Page, M. J., et al. 2010, A&A, 510, A35

Mateos, S., Alonso-Herrero, A., Carrera, F. J., et al. 2012, MNRAS, 426, 3271
Mushotzky, R. 2004, in Supermassive Black Holes in the Distant Universe, ed. A. J. Barger, Astrophys. Space Sci. Lib., 308, 53
Nenkova, M., Ivezić, Ž., & Elitzur, M. 2002, ApJ, 570, L9
Nenkova, M., Sirocky, M. M., Nikutta, R., Ivezić, Ž., & Elitzur, M. 2008, ApJ, 685, 160
Neugebauer, G., Oke, J. B., Becklin, E. E., et al. 1979, ApJ, 230, 79
Page, M. J., McHardy, I. M., Gunn, K. F., et al. 2003, Astron. Nachr., 324, 101
Pérez García, A. M., Rodríguez Espinosa, J. M., & Santolaya Rey, A. E. 1998, ApJ, 500, 685
Pérez-González, P. G., Rieke, G. H., Villar, V., et al. 2008, ApJ, 675, 234
Perola, G. C., Puccetti, S., Fiore, F., et al. 2004, A&A, 421, 491
Pineau, F.-X., Motch, C., Carrera, F., et al. 2011, A&A, 527, A126
Ramos Almeida, C., Levenson, N. A., Alonso-Herrero, A., et al. 2011, ApJ, 731, 92
Ranalli, P., Comastri, A., Vignali, C., et al. 2013, A&A, 555, A42
Rieke, G. H., & Lebofsky, M. J. 1981, ApJ, 250, 87
Rieke, G. H., Young, E. T., Engelbracht, C. W., et al. 2004, ApJS, 154, 25
Schurch, N. J., Roberts, T. P., & Warwick, R. S. 2002, MNRAS, 335, 241
Steidel, C. C., Hunt, M. P., Shapley, A. E., & et al. 2002, ApJ, 576, 653
Stern, D., Eisenhardt, P., Gorjian, V., et al. 2005, ApJ, 631, 163
Stern, D., Assef, R. J., Benford, D. J., et al. 2012, ApJ, 753, 30
Stevens, J. A., Page, M. J., Ivison, R. J., et al. 2005, MNRAS, 360, 610
Szokoly, G. P., Bergeron, J., Hasinger, G., et al. 2004, ApJS, 155, 271
Tozzi, P., Gilli, R., Mainieri, V., et al. 2006, A&A, 451, 457
Treister, E., & Urry, C. M. 2005, ApJ, 630, 115
Treister, E., Urry, C. M., & Virani, S. 2009, ApJ, 696, 110
Ueda, Y., Akiyama, M., Ohta, K., & Miyaji, T. 2003, ApJ, 598, 886
Urry, C. M., & Padovani, P. 1995, PASP, 107, 803
Wall, J. V., & Jenkins, C. R. 2008, Practical Statistics for Astronomers, 21
Werner, M. W., Roellig, T. L., Low, F. J., et al. 2004, ApJS, 154, 1
Worsley, M. A., Fabian, A. C., Barcons, X., et al. 2004, MNRAS, 352, L28
Worsley, M. A., Fabian, A. C., Bauer, F. E., et al. 2005, MNRAS, 357, 1281
Xue, Y. Q., Luo, B., Brandt, W. N., et al. 2011, ApJS, 195, 10
Xue, Y. Q., Wang, S. X., Brandt, W. N., et al. 2012, ApJ, 758, 129
Yan, L., Donoso, E., Tsai, C.-W., et al. 2013, AJ, 145, 55
Yaqoob, T. 1997, ApJ, 479, 184